

# Stability of cloud-topped boundary layers

By HUNG-CHI KUO and WAYNE H. SCHUBERT

*Department of Atmospheric Science, Colorado State University, Fort Collins, Colorado 80523*

(Received 30 June 1987; revised 12 January 1988)

## SUMMARY

According to the thermodynamic theory of cloud top evaporative instability, persistent stratocumulus should be observed only when the cloud top jumps in equivalent potential temperature  $\theta_e$  and total water mixing ratio  $r$  satisfy the stability condition  $\Delta\theta_e > k(L/c_p)\Delta r$ , where  $k \approx 0.23$ . Using observations of persistent mid-latitude and subtropical stratocumulus we find that the above stability condition is violated in many cases. In an attempt to understand how stratocumulus can persist under apparently unstable conditions we first review the thermodynamic instability theory and then develop a dynamical framework using a two-dimensional Boussinesq moist convection model with spectral discretization and with resolution sufficient to simulate cloud top processes. Idealized initial value experiments confirm that, when the above condition is violated, evaporative instability leads to cloud breakup through sequential dissections of existing cloud. However, initial conditions close to the critical stability line (e.g.  $\Delta\theta_e, (L/c_p)\Delta r = -6\text{ K}, -15\text{ K}$ ) lead to cloud breakup with a characteristic cloud half-life of several hours, while physically realistic initial conditions far from the critical stability line (e.g.  $\Delta\theta_e, (L/c_p)\Delta r = -16\text{ K}, -25\text{ K}$ ) lead to more rapid breakup, with a cloud half-life on the order of 1/2 hour. When evaporative instability is so weak that the associated cloud half-life is as long as several hours, other physical processes (such as surface evaporation) can apparently moisten the boundary layer rapidly enough to mask the cloud breakup process.

## 1. INTRODUCTION

In a paper which has become a classic, Lilly (1968) constructed a simple model of the shallow, cloud-topped boundary layers which form under strong subsidence inversions associated with subtropical and mid-latitude high pressure systems. Using concepts similar to those developed by Squires (1958) for penetrative downdraughts in cumulus clouds, Lilly argued that one of the theoretical requirements for applicability of his model was the stability of cloud top against penetration by dry upper air masses. According to this argument, cloud top instability could be understood as follows: "If a parcel of the upper air is introduced into the cloud layer and mixed by turbulence, evaporation of cloud droplets into the dry parcel will reduce its temperature. If the mixed parcel reaches saturation at a lower temperature than that of the cloud top it will be negatively buoyant and can then penetrate freely into the cloud mass. In such a case the evaporation and penetration process will occur spontaneously and increase unstably until the cloud is evaporated." Since the condition for no change in temperature upon evaporative mixing (while maintaining saturation) is that the equivalent potential temperatures of the wet and dry layers be equal, Lilly concluded that for stability of a cloud layer the temperature inversion must be strong enough that the equivalent potential temperature remains constant or increases upwards at cloud top. Defining the jump operator  $\Delta$  as the above-cloud value minus the in-cloud value, this condition for stability can be written

$$\Delta\theta_e > 0. \quad (1)$$

Near the end of his paper Lilly presented three radiosonde soundings taken in August 1962 at Oakland, California during stratus overcast conditions. The soundings showed that the warm, dry air above the inversion had an equivalent potential temperature about 5 to 9 K higher than the cool, moist boundary layer air. Lilly concluded that the prediction of a positive  $\Delta\theta_e$  "seems to agree with the observational data".

Although the mixed layer model equation set proposed by Lilly took into account the effects of water vapour and liquid water on buoyancy, his cloud top stability analysis did not. Randall (1980) and Deardorff (1980a) included these additional buoyancy effects and proposed what they considered to be the more accurate stability condition

$$\Delta\theta_e > k(L/c_p)\Delta r \quad (2)$$

where  $\Delta r$  is the cloud top jump in total (vapour plus liquid) water mixing ratio and  $k$  is a dimensionless parameter which has the typical value  $k = 0.23$ . In section 2 we shall give a derivation of Eq. (2). For now we simply note that, under typical stratocumulus conditions,  $\Delta r < 0$  so that the stability criterion (2) is not as strict as (1) in the sense that it predicts cloud top stability even when  $\Delta\theta_e$  is slightly negative.

The stability criterion (2) divides the  $(\Delta\theta_e, \Delta r)$  plane as shown in Fig. 1. If (2) is a sharp stability condition, we might expect that all soundings taken in *persistent* stratocumulus conditions would have associated  $(\Delta\theta_e, \Delta r)$  values which lie to the right of the critical line. Indeed, the three Oakland soundings analysed by Lilly do lie far to the right of this line. We might also expect that soundings taken near the boundary between the stratocumulus regime and the trade cumulus regime would be characterized by points close to or just to the left of the stability line. One might imagine boundary layer air flowing equatorward around the east side of the subtropical high pressure cell over

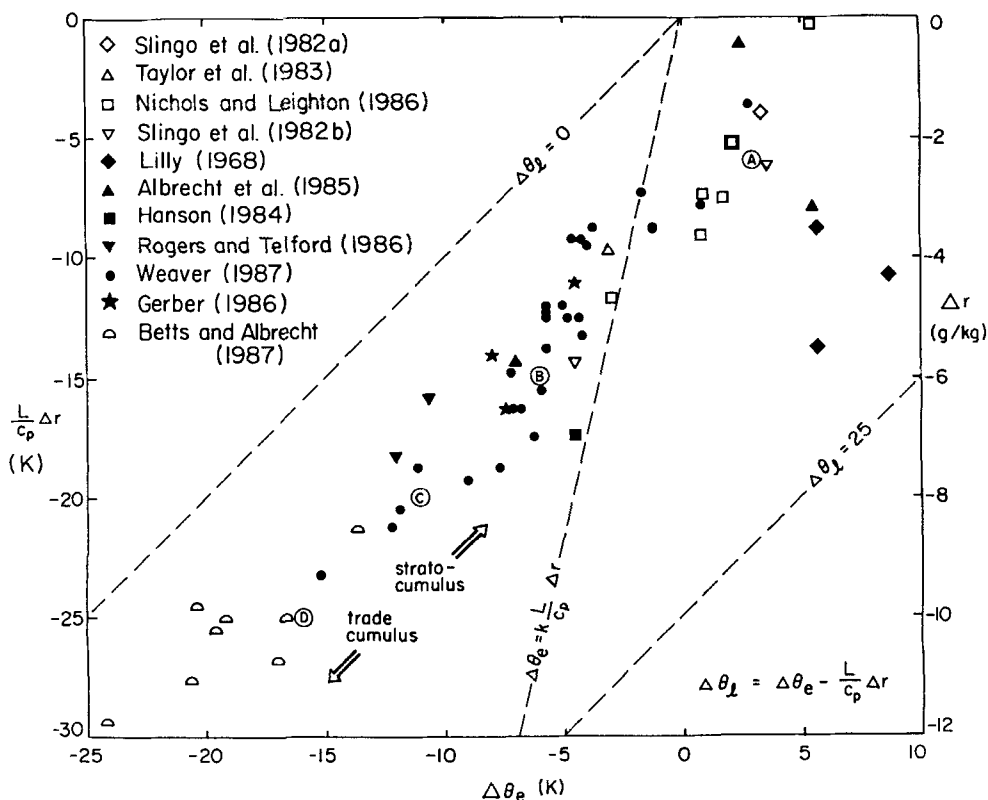


Figure 1. The  $(\Delta\theta_e, \Delta r)$  plane, with the critical thermodynamic instability curve ( $\Delta\theta_e = k(L/c_p)\Delta r$ ). Observational data are indicated by the coded symbols, with open symbols for mid-latitude cases, solid symbols for subtropical cases and 'cumulus symbols' for trade cumulus cases. Two thirds of the stratocumulus observations lie to the left of the critical curve and hence are at odds with the predictions of the thermodynamic theory of cloud top entrainment instability.

increasingly warmer water, with boundary layer values of  $\theta_e$  increasing faster than above-cloud values, so that soundings eventually cross from the stable to the unstable side of the critical stability line and cloud patterns change from stratocumulus to trade cumulus.

It was perhaps with the above expectations in mind that many have witnessed with some surprise an increasing number of observations of apparently persistent stratocumulus conditions with associated  $(\Delta\theta_e, \Delta r)$  values which violate the stability condition (2). This set of stratocumulus observations, which has accumulated over the last ten years, can be divided into two subsets: aircraft, tethered balloon and shipboard sounding data taken in *mid-latitude* stratocumulus over England and over the surrounding waters of the North Atlantic and the North Sea; and aircraft and tethered balloon data taken along and off the California coast in the *subtropical* marine stratocumulus regime of summer and fall. This data base is described in the nine papers summarized in the top two sections of Table 1. We have examined this data set with the objective of documenting

TABLE 1. A BRIEF SUMMARY OF THE DATA USED IN FIG. 1

Reference	Location	Date	Comments
<i>Mid-latitude stratocumulus</i>			
Slingo <i>et al.</i> (1982a)	Near 60°N 10°W	8 August 1978	Three aircraft during JASIN
Taylor <i>et al.</i> (1983)	Ship triangle centred at 59°N 12°W	31 August 1978	Radiosondes at 1 to 2 hour intervals during JASIN
Nicholls and Leighton (1986)	U.K. coastal waters, primarily North Sea	27 April, 22 and 29 July 1982, 15 December 1982, 2, 16 November 1983	MRF C-130 flights, some into layers decoupled from the surface
Slingo <i>et al.</i> (1982b)	Cardington, U.K.	26–27 October 1977, 15 January 1978	Tethered balloon flights into nocturnal stratocumulus
<i>Subtropical stratocumulus</i>			
Albrecht <i>et al.</i> (1985)	Near 35°N 125°W	5, 13, 17 June 1976	Three NCAR Electra flights from NASA Ames
Hanson (1984)	Near 29°N 122°W	27 June 1981	NOAA WP-3D flights from San Diego
Rogers and Telford (1986)	About 100 km west of San Francisco	25 August 1982	Seven of eight NCAR Queen Air soundings showed $\Delta\theta_e < 0$ . Soundings S7 and S9 are shown in Fig. 1.
Weaver (1987)	About 500 km south-west of San Diego	30 July to 21 August 1985	Ten NCAR Electra flights from San Diego
Gerber (1986)	San Nicolas Island, California	18–29 October 1984	Naval Research Laboratory tethered balloon flights into stratocumulus overcast (flights 12, 17, 18)
<i>Trade cumulus</i>			
Betts and Albrecht (1987)	Near 15°N 56°W	22–26 June 1969	Radiosondes at 1.5-hour intervals during BOMEX
	Near 11°N 38°W	7–12 February 1969	Radiosondes at 3-hour intervals during ATEX
	Between Hawaii and the equator	15 January to 20 February 1979	Dropwindsondes during FGGE

the  $(\Delta\theta_e, \Delta r)$  values of soundings through persistent stratocumulus decks. In addition we have made use of trade cumulus data from shipboard soundings in the Atlantic during BOMEX (Holland and Rasmusson 1973) and ATEX (Augstein *et al.* 1973), and from FGGE dropwindsonde data south of Hawaii, all of which have been analysed by Betts and Albrecht (1987). For the trade cumulus cases we have defined the  $\Delta$  operator as the above-trade-inversion value minus the subcloud layer value, which would be equivalent to a jump across the trade inversion if the convective layer (cloud layer plus subcloud layer) were uniformly mixed. The results of this survey of stratocumulus and trade cumulus data are given by the fifty-six coded symbols shown in Fig. 1, with the eight 'cumulus symbols' near the lower left denoting the trade cumulus data from Betts and Albrecht, the closed symbols denoting the subtropical stratocumulus cases and the remaining open symbols the mid-latitude stratocumulus cases. Two interesting aspects of this diagram are the approximate arrangement of the points along a  $\Delta\theta_i = 9\text{ K}$  line (where  $\Delta\theta_i = \Delta\theta_e - (L/c_p)\Delta r$ ) and the fact that two thirds (thirty-two out of forty-eight) of the stratocumulus cases violate condition (2). The worst offenders are the subtropical cases, especially those taken by the NCAR Electra south-west of San Diego during July and August 1985 (Weaver 1987). As examples consider the points for which  $(\Delta\theta_e, \Delta r) = (-11\text{ K}, -7.5\text{ g kg}^{-1})$  and  $(-12\text{ K}, -8\text{ g kg}^{-1})$ . The  $\theta_e$  profiles for these cases (1757 and 2233 GMT 9 August 1985, respectively) are shown in Fig. 2. High resolution GOES images at 1803 and 2333 GMT from the CSU ground station are shown in Fig. 3, confirming the persistence of this extensive cloud deck. Although the GOES images depict a cellular cloud pattern, a review of film from the Electra side-viewing movie cameras reveals that breaks in the stratocumulus were very rare so that the fractional cloudiness in this case was essentially 100%.

Further data relevant to the cloud top evaporative instability theory were recently acquired as part of the FIRE marine stratocumulus field project. From a site on the north-west tip of San Nicolas Island, California, during the period 30 June to 19 July 1987, Schubert *et al.* (1987a, b) obtained sixty-nine high vertical resolution (about 15 m) radiosonde soundings and a nearly continuous laser ceilometer record of stratocumulus cloud base height. The ceilometer record shows that the 30 June to 19 July period can be characterized as quite cloudy, with fifty-five of the sixty-nine soundings being released with stratocumulus overhead. For each of these fifty-five soundings we have determined the cloud top total water jump  $\Delta r$  as follows. We first compute the vertically averaged water vapour mixing ratio in the layer which extends from 60 m to 240 m above cloud top. We then subtract from this the average water vapour mixing ratio in the layer which extends from 65 m to 165 m above sea level (the island sounding site being 38 m above sea level). This water vapour mixing ratio difference should be equivalent to the cloud top jump in total water if the boundary layer is well mixed. The procedure for determining  $\Delta\theta_e$  is identical. In this way each of the fifty-five soundings was characterized by a point in the  $(\Delta\theta_e, \Delta r)$  plane as shown in Fig. 4. As can be seen, forty of the fifty-five points lie on the stable side of the thermodynamic stability line while fifteen lie on the unstable side. According to the ceilometer record, seven of the unstable cases show cloud breakup within twelve hours while four of the stable cases show breakup within twelve hours. The cases exhibiting breakup are indicated in Fig. 4 by the partially blackened symbols, with the fraction of blackening indicating the fraction of twelve hours before cloud disappearance. The occurrence of eight fully blackened symbols on the unstable side of the critical stability line reaffirms our previous conclusion that persistent cloudiness is possible under unstable conditions. The occurrence of partially blackened symbols on the stable side of the critical stability line indicates that cloud top evaporative instability is not the only mechanism for breakup.

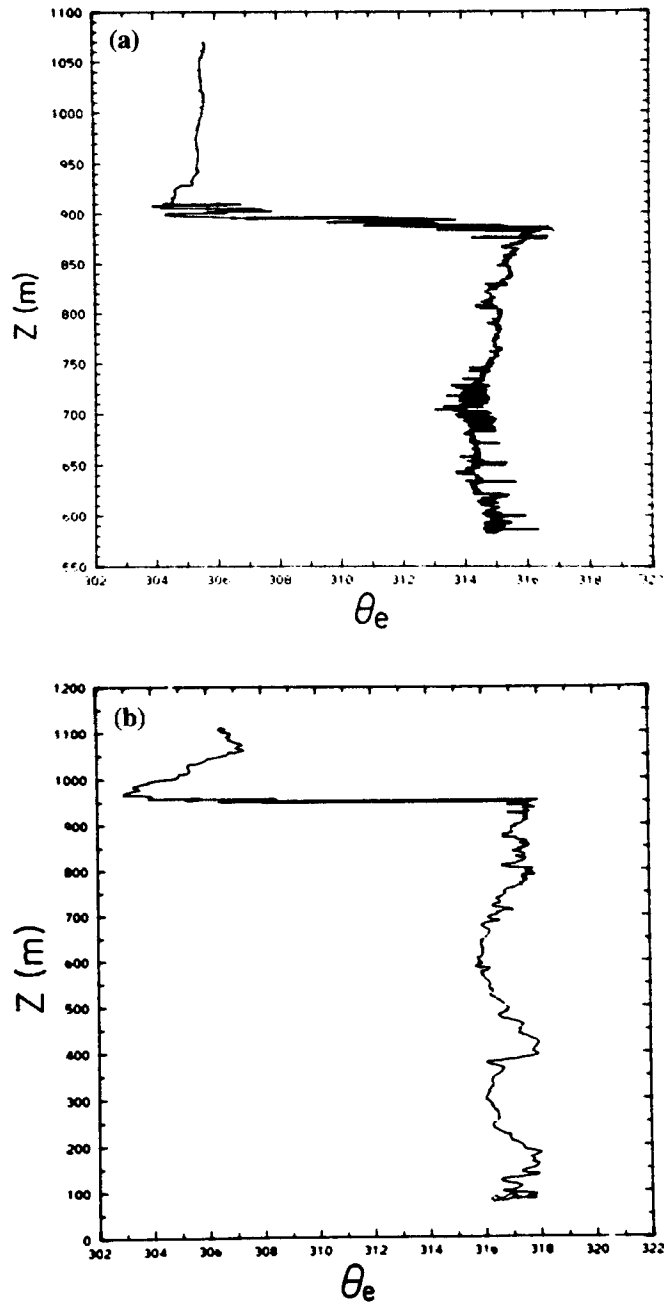


Figure 2. The  $\theta_e$  soundings at 1757 (a) and 2233 (b) GMT 9 August 1985 associated with the stratocumulus fields shown in Fig. 3.

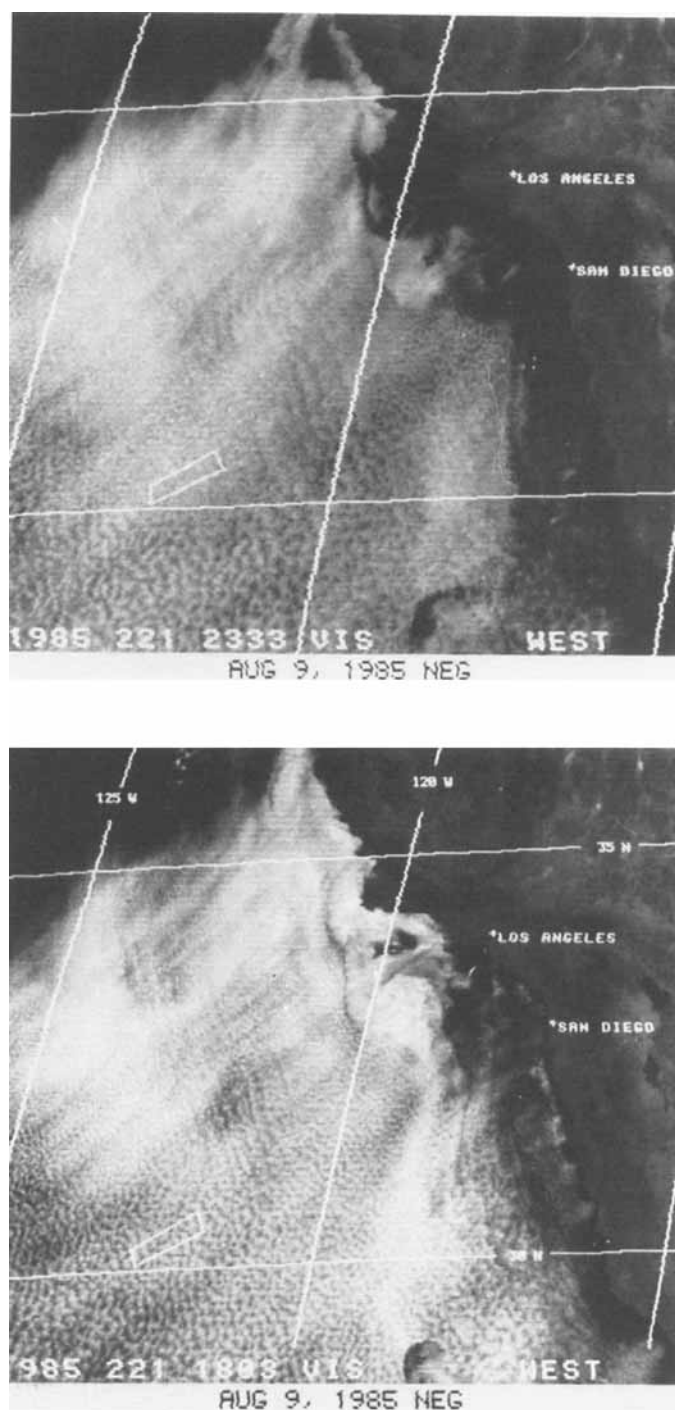


Figure 3. GOES visible images for 1803 (upper) and 2333 (lower) GMT 9 August 1985. The box indicates the area of aircraft observations from which the soundings shown in Fig. 2 were obtained.

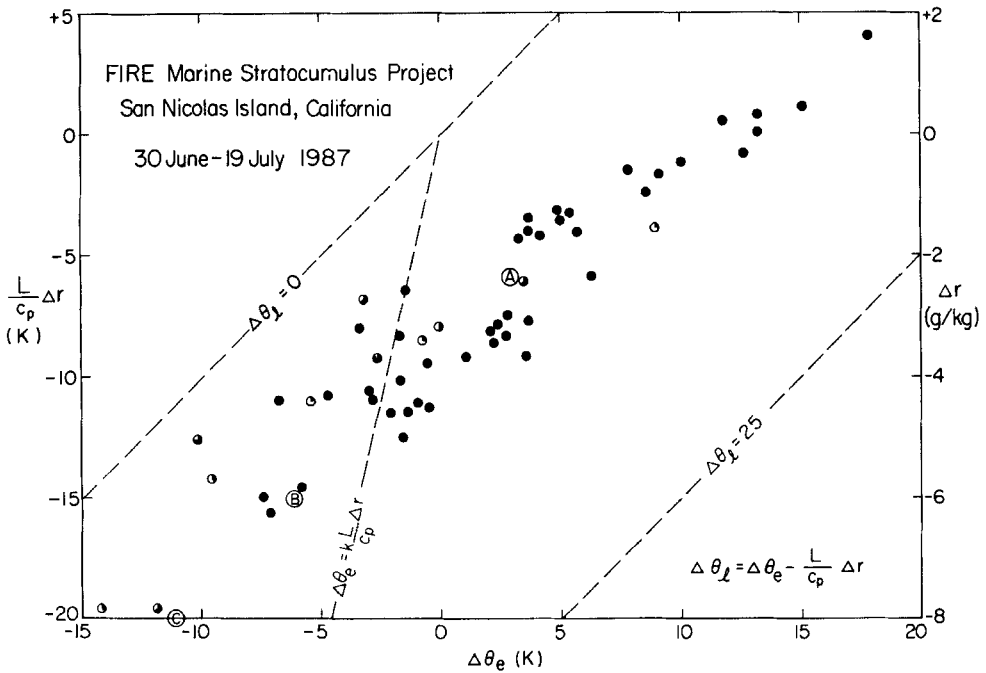


Figure 4. The  $(\Delta\theta_e, \Delta r)$  plane, with the critical thermodynamic instability curve ( $\Delta\theta_e = k(L/c_p)\Delta r$ ). Plotted points have been obtained from fifty-five high vertical resolution soundings taken during stratocumulus conditions on San Nicolas Island, California during the period 30 June to 19 July 1987. The cases exhibiting breakup are indicated by the partially blackened symbols, with the fraction of blackening indicating the fraction of twelve hours before cloud disappearance. Fully blackened symbols indicate that conditions remained cloudy for at least twelve hours. Note the existence of persistent stratocumulus under conditions which are unstable according to the thermodynamic theory of evaporative instability.

Because of the existence of persistent cloudiness under unstable conditions, one might reasonably question whether evaporative instability actually exists or, if it does, whether it possesses rapid enough growth rates to be of physical significance. In the remainder of this paper we shall attempt to address these questions. In section 2 we perform a more thorough thermodynamical analysis which demonstrates the dependence of the buoyancy of Lilly's mixed parcel on the relative masses of the original two unmixed parcels. The relative masses ( $\chi$  in the equation set (3)–(9)) remain an undetermined parameter in the thermodynamic theory. In section 3 we introduce what we consider to be the simplest dynamical model capable of removing this arbitrariness in the choice of  $\chi$ . Thus, section 3 takes us from the realm of thermodynamic theories of evaporative instability into the realm of dynamic theories. We can then perform integrations in which we perturb initial soundings which are judged to be unstable according to the thermodynamic theory. In section 4 we describe experiments based on initial soundings associated with the four points labelled A to D in Fig. 1. These results confirm the existence of evaporative instability. At the same time they give estimates for the dependence of the time scale and life cycle of the instability on the cloud top jumps in  $\theta_e$  and  $r$ , thereby providing a basis for interpreting the data in Figs. 1 and 4.

## 2. THERMODYNAMIC THEORY OF CLOUD TOP EVAPORATIVE INSTABILITY

In order to better understand the thermodynamic theory of cloud top instability we now follow an argument similar to that given by Albrecht *et al.* (1985) and Nicholls and Turton (1986). Consider a unit mass mixture consisting of  $\chi$  mass units of warm dry air from just above the inversion and  $1 - \chi$  mass units of cool moist air from just below the inversion. Using the subscripts a and b to denote respectively the above-inversion parcel and the below-inversion parcel, we obtain

$$\theta_c = \chi\theta_{ca} + (1 - \chi)\theta_{cb} = \theta_{cb} + \chi\Delta\theta_c \quad (3)$$

and

$$r = \chi r_a + (1 - \chi)r_b = r_b + \chi\Delta r \quad (4)$$

for the equivalent potential temperature  $\theta_c$  and the total water mixing ratio  $r$  of the mixed parcel. If we also know the height,  $z$ , of the mixed parcel, we can use the Boussinesq version of the theory of moist convection (Ogura and Phillips 1962) to obtain the potential temperature  $\theta$ , the water vapour mixing ratio  $q$ , the saturation water vapour mixing ratio  $q^*$  and the liquid water mixing ratio  $l$  from the four equations

$$\theta = \theta_c - (L/c_p)q \quad (5)$$

$$q^* = \bar{q}^* \exp \left\{ \frac{L}{R_v \theta_0} \left( \frac{\theta - \theta_0}{\theta_0} \right) \right\} \quad (6)$$

$$(q, l) = \begin{cases} (q^*, r - q^*) & r > q^* \\ (r, 0) & r \leq q^* \end{cases} \quad (7)$$

$$(q, l) = \begin{cases} (q^*, r - q^*) & r > q^* \\ (r, 0) & r \leq q^* \end{cases} \quad (8)$$

Here  $L$  is the constant latent heat of condensation,  $R_v$ , the gas constant for water vapour,  $\theta_0$  a constant reference potential temperature,  $\bar{q}^*(z) = 0.622e^*(\bar{T}(z))/p_0$ , a known function of  $z$ ,  $p_0 = 100$  kPa, and  $\bar{T}(z) = \theta_0 - gz/c_p$ . For the present calculations we have chosen  $\theta_0$  to be 288.15 K and have used Tetens's formula for the saturation vapour pressure  $e^*$ . To actually solve (5)–(8) for  $\theta, q, q^*, l$  from given  $z, \theta_c, r$  we can proceed as follows. First assume the second alternative in (7, 8), i.e.  $r \leq q^*$  and  $(q, l) = (r, 0)$ , so that  $\theta$  can be computed from (5) with  $q$  replaced by  $r$ . Next compute  $q^*$  from (6) and check to see if  $r \leq q^*$ , as originally assumed. If a contradiction is reached, we conclude that  $r > q^*$ ; we must then iteratively adjust  $\theta, q$  (which now equals  $q^*$ ) and  $l$  until we obtain the solution of (5), (6) and the first alternative in (7, 8). A rapidly convergent refined Newton scheme for doing this is discussed in section 3. After solving (5)–(8) we can compute the mixed parcel's virtual potential temperature  $\theta_v$  from

$$\theta_v = \theta + \theta_0(\delta q - l) \quad (9)$$

where  $\delta = 0.608$ . From a comparison of  $\theta_v$  with  $\theta_{vb}$  we can predict whether the mixed parcel is likely to rise or sink. Thus, (3)–(9) form the basis for the thermodynamic theory of cloud top entrainment instability.

Now consider  $\theta_{cb} = 316$  K,  $r_b = 10.5$  g kg<sup>-1</sup> and

$$(\Delta\theta_c, (L/c_p)\Delta r) = \begin{cases} (3\text{ K}, -6\text{ K}) & \text{for case A} \\ (-6\text{ K}, -15\text{ K}) & \text{for case B} \\ (-11\text{ K}, -20\text{ K}) & \text{for case C} \\ (-16\text{ K}, -25\text{ K}) & \text{for case D.} \end{cases} \quad (10)$$



Note that all these cases have cloud top liquid water contents of  $0.38 \text{ g kg}^{-1}$ , that they all lie along the  $\Delta\theta_l = 9 \text{ K}$  line in Figs. 1 and 4, and that only case A satisfies (2). Using the above values in the right-hand sides of (3) and (4), and then solving (5)–(9), we obtain the four curves shown in Fig. 5. The kinks in these curves occur when  $\chi$  becomes large enough that the mixed parcel is no longer saturated, i.e. where the solution switches from the first to the second alternative in (7, 8). For sounding A there is apparently no value of  $\chi$  between zero and unity which will lead to negative buoyancy of the mixed parcel. On the contrary, for soundings B to D small values of  $\chi$  lead to negative buoyancy and perhaps to instability, if such small values of  $\chi$  are naturally selected by the dynamics. Although the four curves in Fig. 5 were all obtained with a cloud top liquid water content of  $0.38 \text{ g kg}^{-1}$ , the curves for higher liquid water contents are similar except that the kinks are shifted to larger values of  $\chi$ , which allows for larger negative buoyancy in the unstable cases.

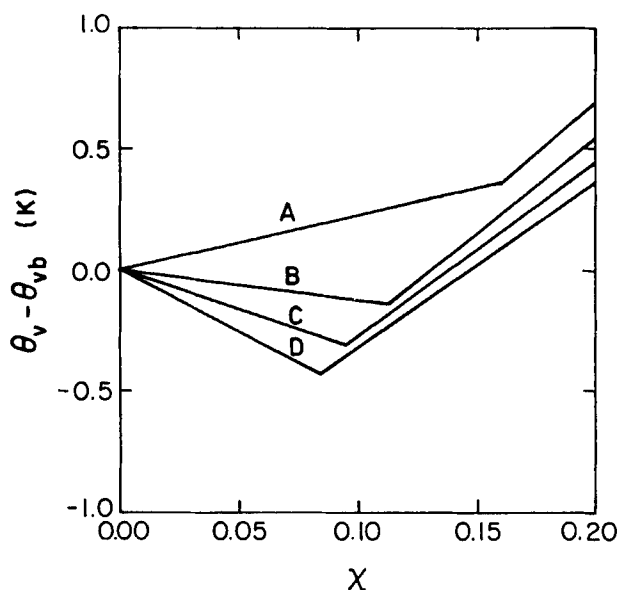


Figure 5. The  $\theta_v$  difference against the fraction ( $\chi$ ) of the unsaturated air involved in the mixture for cases A, B, C and D. The mixing ratio of liquid water content in the cloudy parcel is  $0.38 \text{ g kg}^{-1}$ .

In order to derive (2) from (3)–(9) we now attempt to find an analytical approximation for the buoyancy  $\theta_v - \theta_{vb}$  when  $\chi \leq \hat{\chi}$ , with  $\hat{\chi}$  denoting the smallest value of  $\chi$  which causes the liquid water content of the mixed parcel to vanish. Using (4) and (9) we obtain

$$\theta_v - \theta_{vb} = \theta - \theta_b + \theta_o \{ (1 + \delta)(q - q_b) - \chi \Delta r \}. \quad (11)$$

For  $\chi \leq \hat{\chi}$ ,  $q$  and  $q_b$  are saturation values given in terms of  $\theta$  and  $\theta_b$  by (6). If we approximate the right-hand side of (6) by the first two terms in its Taylor series expansion about  $\theta = \theta_b$  we obtain

$$(L/c_p)(q^* - q_b^*) = \gamma(\theta - \theta_b) = \{ \gamma / (1 + \gamma) \} (\theta_c - \theta_{cb}) \quad (12)$$

where  $\gamma = (L/c_p) \partial q^* / \partial \theta$ . Using (3) and (12) in (11) we obtain

$$\frac{\theta_v - \theta_{vb}}{\theta_o} = \chi \left( \frac{c_p}{Lk} \Delta \theta_c - \Delta r \right) \quad (13)$$

where

$$k = \frac{(1 + \gamma) c_p \theta_o / L}{1 + (1 + \delta) \gamma c_p \theta_o / L} \approx 0.23.$$

If the term within the parentheses of (13) is negative, all mixtures with  $0 < \chi \leq \hat{\chi}$  will be negatively buoyant. On the other hand, if the term within the parentheses is positive, we conclude that there will be no mixture which is negatively buoyant. Thus, according to the thermodynamic theory of evaporative instability, (2) is the condition for stability of a cloud-topped mixed layer.

Why should the predictions of the seemingly plausible thermodynamic theory of cloud top evaporative instability be at odds with observations? Is it possible that the small values of  $\chi$  required for instability are somehow precluded by the dynamics? To answer these questions we must remove the arbitrariness in the specification of  $\chi$  and thereby formulate a closed physical argument. This requires that (3) and (4) be replaced by the conservation laws for  $\theta_e$  and  $r$  while the  $\chi$  parameter is removed by the information content in the momentum equations. Unfortunately, this makes the mathematical problem complicated enough that analytical progress is difficult. This leaves numerical simulation as a reasonable alternative. In the remainder of this paper we shall describe the simplest possible two-dimensional dynamical formulation which can replace (3)–(9). We shall then compare numerical simulations based on the four initial states associated with the points A to D in Fig. 1. The reader who is not interested in the details of the dynamical model may wish to skip directly to section 4, where the numerical results are presented.

### 3. TWO-DIMENSIONAL BOUSSINESQ MODEL

#### (a) Governing equations

The starting point for our model is the formal scale analysis of Ogura and Phillips (1962), who derived the anelastic equations under the assumptions that the percentage range of potential temperature is small and the time scale is set by the Brunt–Väisälä frequency. The anelastic equations reduce to the Boussinesq equations under the additional assumption that the vertical scale of motion is small compared with the depth of an isentropic atmosphere. Since the above assumptions are justified for the marine boundary layer problem, we shall use Ogura and Phillips' Boussinesq equations for shallow moist convection. If the flow is constrained to be two-dimensional we can write these equations in the vorticity/streamfunction form

$$\left. \begin{aligned} \partial^2 \psi / \partial x^2 + \partial^2 \psi / \partial z^2 &= \zeta \\ \psi(x, 0, t) = \psi(x, H, t) &= 0 \end{aligned} \right\} \quad (14)$$

$$\frac{\partial \zeta}{\partial t} + \frac{\partial}{\partial x} \left( -\frac{\partial \psi}{\partial z} \zeta \right) + \frac{\partial}{\partial z} \left( \frac{\partial \psi}{\partial x} \zeta \right) - \frac{g}{\theta_o} \frac{\partial \theta_v}{\partial x} = \mathcal{F} \quad (15)$$

$$\frac{\partial \theta_e}{\partial t} + \frac{\partial}{\partial x} \left( -\frac{\partial \psi}{\partial z} \theta_e \right) + \frac{\partial}{\partial z} \left( \frac{\partial \psi}{\partial x} \theta_e \right) = \mathcal{G} \quad (16)$$

$$\frac{\partial r}{\partial t} + \frac{\partial}{\partial x} \left( -\frac{\partial \psi}{\partial z} r \right) + \frac{\partial}{\partial z} \left( \frac{\partial \psi}{\partial x} r \right) = \mathcal{H} \quad (17)$$

$$\theta = \theta_e - (L/c_p)q \quad (18)$$

$$q^* = \bar{q}^* \exp \left\{ \frac{L}{R_v \theta_o} \left( \frac{\theta - \theta_o}{\theta_o} \right) \right\} \quad (19)$$

$$(q, l) = \begin{cases} (q^*, r - q^*) & r > q^* \\ (r, 0) & r \leq q^* \end{cases} \quad (20)$$

$$\theta_v = \theta + \theta_o(\delta q - l). \quad (22)$$

This is a closed system in  $\psi$ ,  $\zeta$ ,  $\theta$ ,  $\theta_c$ ,  $\theta_v$ ,  $q$ ,  $q^*$ ,  $l$  and  $r$ , where  $\psi$  and  $\zeta$  are the streamfunction and vorticity,  $\theta$  the potential temperature,  $\theta_c$  the equivalent potential temperature,  $\theta_v$  the virtual potential temperature,  $q$  and  $q^*$  the mixing ratio and saturation mixing ratio of water vapour,  $l$  the mixing ratio of liquid water, and  $r$  the mixing ratio of total water (vapour plus liquid). The terms  $\mathcal{F}$ ,  $\mathcal{G}$  and  $\mathcal{H}$  represent processes on unresolvable scales and will be discussed below. The effects of both water vapour and liquid water on buoyancy are included in (22) and in the last term on the right-hand side of (15). After prediction of  $\theta_c$  and  $r$  from (16) and (17), iteration is required to diagnose  $\theta$ ,  $q$ ,  $q^*$  and  $l$  from (18)–(21). Finally, by comparing (3)–(9) with (14)–(22), we note that the thermodynamic theory's mixing relations (3)–(4) are replaced by the dynamic theory's vorticity and conservation relations (14)–(17).

We shall solve (14)–(22) on the domain  $0 \leq x \leq L$ ,  $0 \leq z \leq H$ , with the assumption that all variables are periodic in  $x$  and  $\psi = 0$  on  $z = 0, H$ . In the following section we discuss an accurate spectral method (Fourier–Chebyshev tau method) for solving the system (14)–(22).

### (b) Space and time discretization

The strong gradients of temperature and moisture which are produced in marine boundary layer convection place great demands on spatial discretization schemes used in simulation models. In the present work we have used a scheme which is spectral in both the horizontal and vertical directions. In the horizontal, Fourier basis functions are used so that the periodicity is built into each basis function. In the vertical, Chebyshev polynomial basis functions are used; the upper and lower boundary conditions are not satisfied by each basis function, but rather by the series as a whole.

The dependent variables  $\psi$ ,  $\zeta$ ,  $\theta_c$ ,  $\theta_v$  and  $r$  are approximated by the series expansions

$$\begin{bmatrix} \psi(x, z, t) \\ \zeta(x, z, t) \\ \theta_c(x, z, t) \\ \theta_v(x, z, t) \\ r(x, z, t) \end{bmatrix} = \sum_{m=-M}^M \sum_{n=0}^N \begin{bmatrix} \hat{\psi}_{mn}(t) \\ \hat{\zeta}_{mn}(t) \\ \hat{\theta}_{emn}(t) \\ \hat{\theta}_{vmn}(t) \\ \hat{r}_{mn}(t) \end{bmatrix} T_n(z') e^{2\pi i m x / L} \quad (23)$$

where the  $T_n(z')$  are the Chebyshev polynomials defined on the interval  $-1 \leq z' \leq 1$  by  $T_n(z') = \cos(n\phi)$  with  $z' = 2z/H - 1 = \cos \phi$ . Let us define the Fourier–Chebyshev inner product of two functions  $f(x, z)$  and  $g(x, z)$  as

$$\langle f, g \rangle = \frac{1}{L} \int_{-1}^1 \int_0^L \frac{f(x, z) g^*(x, z)}{(1 - z'^2)^{1/2}} dx dz' \quad (24)$$

where the  $*$  denotes complex conjugate. The spectral coefficient  $\hat{\psi}_{mn}(t)$  is given by

$$\hat{\psi}_{mn}(t) = \frac{2}{\pi c_n} \langle \psi(x, z, t), T_n(z') e^{2\pi i m x / L} \rangle \quad (25)$$

with

$$c_n = \begin{cases} 2 & n = 0 \\ 1 & n > 0. \end{cases}$$

Similar relations hold for  $\hat{\xi}_{mn}(t)$ ,  $\hat{\theta}_{emn}(t)$ ,  $\hat{\theta}_{vmn}(t)$  and  $\hat{r}_{mn}(t)$ . Equation (25) is the transformation from physical space to Fourier–Chebyshev spectral space and (23) is the transformation back.

The coefficients in (23) are determined by requiring the residual in (15), (16) and (17) to be orthogonal to all the basis functions  $T_n(z') e^{2\pi i m x / L}$  ( $-M \leq m \leq M$  and  $0 \leq n \leq N$ ), the residual in the Poisson equation (14) to be orthogonal to all the basis functions except those for which  $n = N - 1, N$ , and the boundary conditions on  $\psi$  to be satisfied by the series as a whole. Thus, with the nonlinear terms defined by

$$\left. \begin{aligned} A &= -(\partial \psi / \partial z) \zeta & B &= (\partial \psi / \partial x) \zeta \\ C &= -(\partial \psi / \partial z) \theta_c & D &= (\partial \psi / \partial x) \theta_c \\ E &= -(\partial \psi / \partial z) r & F &= (\partial \psi / \partial x) r \end{aligned} \right\} \quad (26)$$

the tau equations are

$$\left. \begin{aligned} \frac{4}{H^2 c_n} \sum_{\substack{p=n+2 \\ p+\text{neven}}}^N p(p^2 - n^2) \hat{\psi}_{mp} - \left( \frac{2\pi m}{L} \right)^2 \hat{\psi}_{mn} &= \hat{\xi}_{mn} \quad (n = 0, 1, 2, \dots, N-2) \\ \sum_{p=0}^N (-1)^p \hat{\psi}_{mp} &= 0 \\ \sum_{p=0}^N \hat{\psi}_{mp} &= 0 \end{aligned} \right\} \quad (27)$$

$$\frac{d\hat{\xi}_{mn}}{dt} + \hat{A}_{mn}^{(1,0)} + \hat{B}_{mn}^{(0,1)} - \frac{g}{\theta_0} \hat{\theta}_{vmn}^{(1,0)} = \hat{\mathcal{F}}_{mn} \quad (28)$$

$$\frac{d\hat{\theta}_{emn}}{dt} + \hat{C}_{mn}^{(1,0)} + \hat{D}_{mn}^{(0,1)} = \hat{\mathcal{G}}_{mn} \quad (29)$$

$$\frac{d\hat{r}_{mn}}{dt} + \hat{E}_{mn}^{(1,0)} + \hat{F}_{mn}^{(0,1)} = \hat{\mathcal{H}}_{mn} \quad (30)$$

where  $\hat{A}_{mn}^{(1,0)}$ ,  $\hat{C}_{mn}^{(1,0)}$ ,  $\hat{E}_{mn}^{(1,0)}$ ,  $\hat{\theta}_{vmn}^{(1,0)}$  are the spectral coefficients of  $\partial A / \partial x$ ,  $\partial C / \partial x$ ,  $\partial E / \partial x$ ,  $\partial \theta_v / \partial x$  and  $\hat{B}_{mn}^{(0,1)}$ ,  $\hat{D}_{mn}^{(0,1)}$ ,  $\hat{F}_{mn}^{(0,1)}$  are the spectral coefficients of  $\partial B / \partial z$ ,  $\partial D / \partial z$ ,  $\partial F / \partial z$ . Likewise  $\hat{\mathcal{F}}_{mn}$ ,  $\hat{\mathcal{G}}_{mn}$  and  $\hat{\mathcal{H}}_{mn}$  are the spectral coefficients of  $\mathcal{F}$ ,  $\mathcal{G}$  and  $\mathcal{H}$ . Some of the

details in the derivation of (27)–(30) are given in the appendix. The relation between  $\hat{A}_{mn}^{(1,0)}$  and  $\hat{A}_{mn}$  (the spectral coefficient of  $A$ ) is

$$\hat{A}_{mn}^{(1,0)} = i(2\pi m/L)\hat{A}_{mn} \quad (31)$$

with similar relations for  $\hat{C}_{mn}^{(1,0)}$ ,  $\hat{E}_{mn}^{(1,0)}$  and  $\hat{\theta}_{mn}^{(1,0)}$ . As discussed in the appendix the relation between  $\hat{B}_{mn}^{(0,1)}$  and  $\hat{B}_{mn}$  (the spectral coefficient of  $B$ ) is

$$\hat{B}_{mn}^{(0,1)} = \frac{4}{Hc_n} \sum_{\substack{p=n+1 \\ p+n \text{ odd}}}^N p\hat{B}_{mp} \quad (32)$$

with similar relations for  $\hat{D}_{mn}^{(0,1)}$  and  $\hat{F}_{mn}^{(0,1)}$ . Although the spectral evaluation of  $z$  derivatives by (32) looks at first sight more difficult than the spectral evaluation of  $x$  derivatives by (31), such is not the case. Equation (32) yields the (backward) recurrence formula

$$c_{n-1}\hat{B}_{m,n-1}^{(0,1)} - \hat{B}_{m,n+1}^{(0,1)} = (4/H)n\hat{B}_{m,n} \quad n = 1, 2, \dots, N-1 \quad (33)$$

with the starting values  $\hat{B}_{m,N+1}^{(0,1)} = \hat{B}_{m,N}^{(0,1)} = 0$ . For fixed  $m$ , the use of (33) allows the  $N$  values of  $\hat{B}_{mn}^{(0,1)}$  to be computed in  $O(N)$  operations. The transform method (Orszag 1970; Eliassen *et al.* 1970) is used in computing the spectral coefficients  $\hat{A}_{mn}$ ,  $\hat{B}_{mn}$ ,  $\hat{C}_{mn}$ ,  $\hat{D}_{mn}$ ,  $\hat{E}_{mn}$  and  $\hat{F}_{mn}$ . To eliminate aliasing error in the quadratic nonlinear terms,  $3M$  points in  $x$  and  $3N/2$  points in  $z$  are needed in the physical domain.

The unresolvable scale processes represented by  $\mathcal{F}$ ,  $\mathcal{G}$  and  $\mathcal{H}$  are handled in spectral space by specifying the terms on the right-hand sides of (28)–(30) in the following way:

$$\left. \begin{aligned} \hat{\mathcal{F}}_{mn} &= -k_x(2\pi m/L)^2 \hat{\xi}_{mn} - k_z(2\pi n/H)^4 \hat{\xi}_{mn} \\ \hat{\mathcal{G}}_{mn} &= -k_x(2\pi m/L)^2 \hat{\theta}_{cmn} - k_z(2\pi n/H)^4 \hat{\theta}_{cmn} \\ \hat{\mathcal{H}}_{mn} &= -k_x(2\pi m/L)^2 \hat{r}_{mn} - k_z(2\pi n/H)^4 \hat{r}_{mn} \end{aligned} \right\} \quad (34)$$

where we have chosen  $k_x = 2.25 \text{ m}^2 \text{ s}^{-1}$  and  $k_z = 10 \text{ m}^4 \text{ s}^{-1}$ . The choice of (34) is the most uncertain aspect of the model. However, it is generally believed (e.g. Machenhauer 1979) that simple scale-selective dissipation such as (34) is required to prevent the spectral blocking associated with cascades to smaller spatial scales. We have performed limited tests of the sensitivity of our results to the numerical values of  $k_x$  and  $k_z$ . These tests show only subtle changes in the results when  $k_x$  and  $k_z$  are varied by factors of two.

In the numerical time integration of the above equations, we must solve (27) at each time step. For a given  $m$  ( $-M \leq m \leq M$ ) we regard (27) as a linear algebraic system in the  $N+1$  unknowns  $\hat{\psi}_{mn}$  ( $0 \leq n \leq N$ ), with known right-hand side  $\hat{\xi}_{mn}$ . The matrix structure of this linear system is upper triangular except for the last two rows, which come from the boundary conditions. There are many possible ways to solve (27), two of which are discussed by Gottlieb and Orszag (1977, pages 119–120). Because (27) holds for each  $m$  separately, direct methods are a reasonable alternative, a situation which does not exist when Chebyshev expansions are used in both directions.

Using simple model equations Fulton and Schubert (1987a, b) have investigated the relative merits of various time differencing schemes for Chebyshev spectral methods. When the time step is limited by accuracy rather than stability (as is apparently the case here), fourth-order schemes are more efficient than second-order schemes. As a general rule Fulton and Schubert have found the fourth-order Runge–Kutta scheme to be the most useful, and it has been used here for the time integration of (28)–(30).

(c) *Condensation and evaporation*

At each point in physical space on the transform grid, we must solve (18)–(21) iteratively. Beginning with the values of  $\theta_c$  and  $r$  predicted from (16) and (17), we first assume that  $r \leq q^*$ . If this assumption leads to a contradiction, we must conclude that  $r > q^*$  and  $q = q^*$ . Then,  $q$  can be eliminated between (18) and (19) to obtain

$$G(\theta) = \theta + \frac{L}{c_p} \bar{q}^* \exp \left\{ \frac{L}{R_v \theta_0} \left( \frac{\theta - \theta_0}{\theta_0} \right) \right\} - \theta_c = 0 \quad (35)$$

which must be solved iteratively for  $\theta$ . If we are at iteration  $\nu + 1$ , two approximations to  $G(\theta) = 0$  are

$$G(\theta^{(\nu)}) + G'(\theta^{(\nu)})(\theta^{(\nu+1)} - \theta^{(\nu)}) = 0 \quad (36)$$

and

$$G(\theta^{(\nu)}) + G'(\theta^{(\nu)})(\theta^{(\nu+1)} - \theta^{(\nu)}) + \frac{1}{2} G''(\theta^{(\nu)})(\theta^{(\nu+1)} - \theta^{(\nu)})^2 = 0 \quad (37)$$

where  $\theta^{(\nu)}$  is the value of potential temperature at iteration  $\nu$  and the prime denotes differentiation with respect to  $\theta$ . If we approximate the last term in (37) by the value of  $\theta^{(\nu+1)} - \theta^{(\nu)}$  determined in (36) we obtain

$$\theta^{(\nu+1)} = \theta^{(\nu)} - \frac{G(\theta^{(\nu)})}{G'(\theta^{(\nu)})} \left\{ 1 + \frac{1}{2} \frac{G''(\theta^{(\nu)})G(\theta^{(\nu)})}{[G'(\theta^{(\nu)})]^2} \right\} \quad (38)$$

which is a refined Newton scheme. The refined Newton scheme finds frequent application in numerical analysis, e.g. in the calculation of Gaussian quadrature points (Davis and Rabinowitz 1984, page 114). It reduces to the ordinary Newton scheme if the second derivative term in the braces is neglected. According to Langlois (1973), the estimation of  $\theta$  by (38) is accurate enough that iteration is not necessary. Our experience is almost as good; we have found that (38) produces a machine accurate solution to (35) in only three iterations even when the initial guess of  $\theta$  is off by 10 K. In the model integrations discussed here we have applied (38) four times at each time step.

(d) *Model parameters*

For the integrations presented here we have chosen the model domain to be 2500 m in the (periodic) horizontal direction and 800 m in the vertical. In the spectral discretization we have chosen  $N = M = 64$ . The transform grid for the calculation of nonlinear and diabatic terms consists of 192 equally spaced points in the horizontal and 96 unequally spaced points in the vertical, giving an approximate resolution of nearly 10 m in each direction. A four-second time step is used in the fourth-order Runge–Kutta time integration. This four-second time step retains the full accuracy of the spatial discretization.

## 4. NUMERICAL EXPERIMENTS

To test the evaporative instability theory we now consider four initial value experiments which isolate the interactions between evaporative cooling and dynamics by neglecting the complicating effects of infrared radiative cooling, large-scale subsidence and sea surface fluxes. The four initial soundings used here are associated with the  $(\Delta\theta_c, \Delta r)$  points labelled A to D in Fig. 1. All four initial soundings consist of a 450 m deep layer with a uniform equivalent potential temperature of 316 K and a uniform total

water mixing ratio of  $10.5 \text{ g kg}^{-1}$ . This produces a cloud layer extending from 225 m to 450 m with liquid water increasing adiabatically with height to a peak value of  $0.38 \text{ g kg}^{-1}$ . Capping this 450 m deep boundary layer is an inversion layer of 100 m depth. The air above the inversion is different in each experiment and has properties such that changes in equivalent potential temperature and total water mixing ratio across the inversion are given by (10). Since  $\Delta\theta_l = 9 \text{ K}$  in all four cases, the strength of the temperature inversion is essentially the same for each case. In order to initiate any existing instability in these four atmospheric states, we superimpose on the soundings a motionless state with a 1 K cold anomaly just below the inversion (e.g. Fig. 6 for case A). Our motivation for this initial condition is that such cold anomalies are continuously produced by radiative cooling near cloud top. In fact, in the absence of other physical processes, cold anomalies such as this could be generated in about 10 minutes by an  $80 \text{ W m}^{-2}$  infrared radiative flux divergence across cloud top.

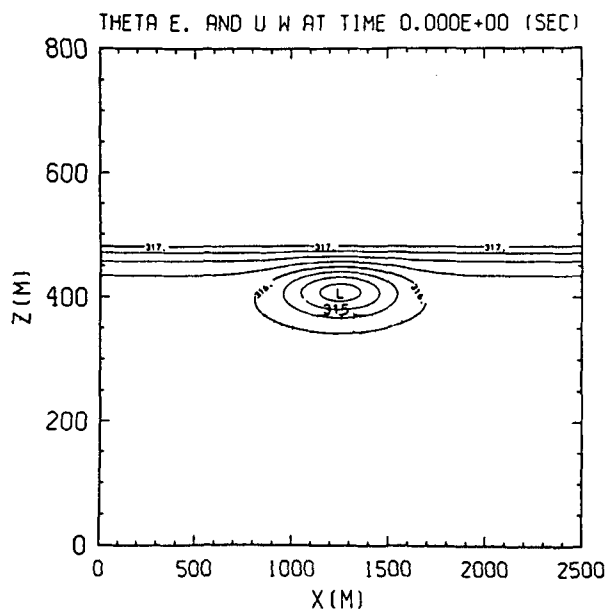


Figure 6. The initial  $\theta_e$  and velocity fields for experiment A.  $\theta_e$  contour intervals as in Fig. 7.

The results from experiments A, B, C and D are shown in Figs. 7 to 10. The  $\theta_e$  fields with a contour interval of  $0.25 \text{ K}$  inside the boundary layer are superimposed on the velocity fields in the upper part of these figures. The lower part shows the cloud liquid water content with a contour interval of  $0.05 \text{ g kg}^{-1}$ . The results from experiment A are presented at 20-minute intervals in Fig. 7. From the  $\theta_e$  and velocity fields we note how the cold bubble sinks to the surface to form symmetric circulations while exciting laterally propagating gravity wave oscillations in the capping inversion. The entrainment associated with the sinking cold fluid leads to low liquid water content in the centre of the domain at 20 minutes (Fig. 7(a)). However, a permanent cloud hole does not form, and the cloud returns to a nearly horizontally homogeneous state at 120 minutes (Fig. 7(f)). This is consistent with thermodynamic theory, which predicts stability for this sounding.

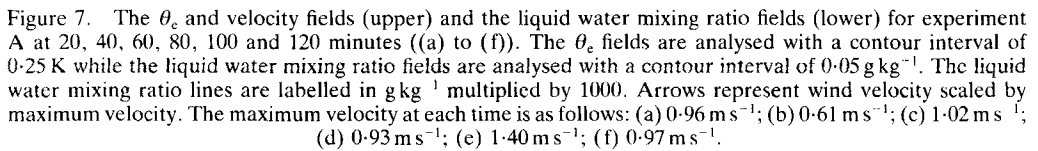
The output of experiment B at 20-minute intervals is shown in Fig. 8. In Fig. 8(a) we see the formation of a narrow cloud hole in the centre of the domain. The hole then shrinks near cloud top and expands near cloud base due to the arrival of the previously entrained air. At 60 minutes the results of experiment B begin to diverge in a fundamental way from those of experiment A. In contrast to experiment A we note that in experiment B two regions of minimum  $\theta_c$  near the cloud top ( $z = 400$  m,  $x = 450$  and  $2050$  m) are generated by gravity waves in the capping inversion at 60 minutes. Because these local minimum  $\theta_c$  regions are inside the cloud (saturated), new regions of entrainment will form. These new regions of entrainment can be clearly seen in the remaining figures (Figs. 8(d), (e) and (f)). Although this apparently confirms the existence of evaporative instability for sounding B, the growth rates in this case are not rapid enough to cause more than a slight decrease in fractional cloud cover in our 120-minute integration.

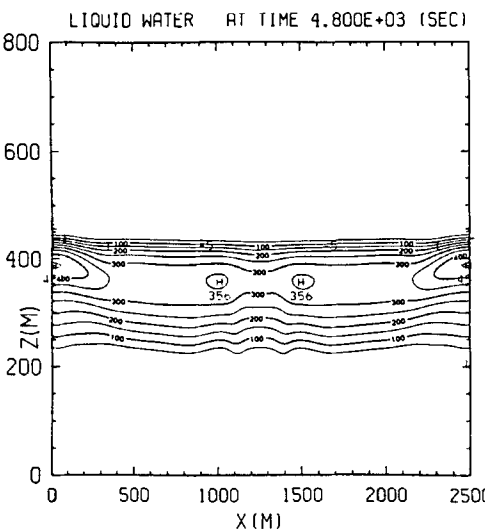
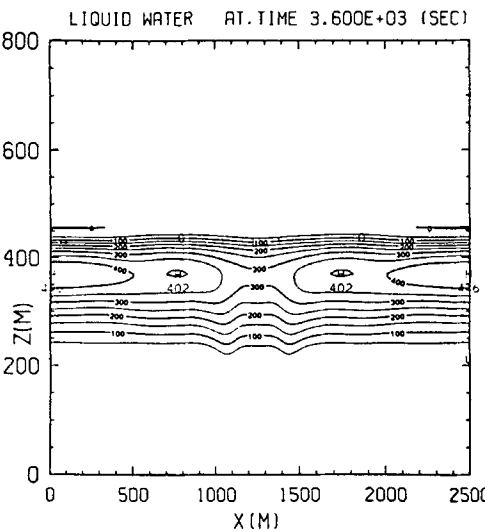
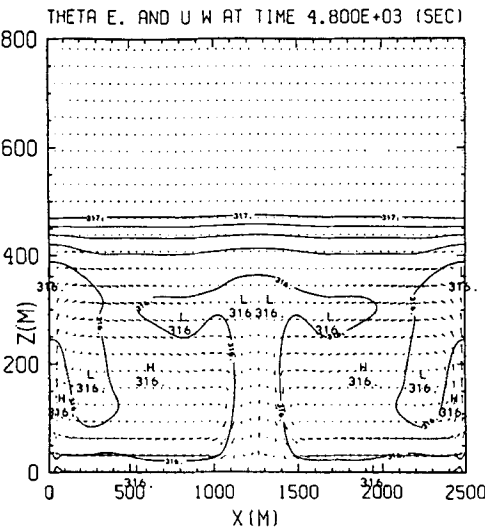
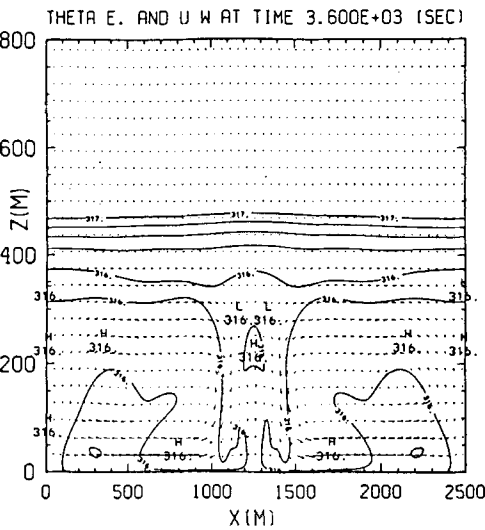
The generation of regions of entrainment by gravity wave oscillations in the inversion as well as the final breakup of stratocumulus can be clearly seen in experiments C and D (Figs. 9 and 10). By comparing corresponding pictures for all the unstable experiments (Figs. 8a, 9a and 10a), we note only subtle differences between experiments B and C while there are already new regions of entrainment generated at 20 minutes in experiment D. Figures 9(b) and 10(b) reveal some similarity between experiments C and D at 60 minutes, i.e. cloud holes in the centre of the domain and several new regions of entrainment. However, there are more regions of entrainment in experiment D than in experiment C. As a result, the cloud in experiment D is thinner and more broken in appearance. Entrainment subsequently breaks the stratocumulus into shallow, weak cumulus (Figs. 9(c) and 10(c)). In these idealized experiments evaporative instability seems to be a process in which large cloudy regions are dissected into smaller cloudy regions with widening clear gaps in between.

It is interesting to note the different breakup times for each of the unstable experiments. If we define the 'cloud half-life' as the time required for half of the total liquid water in the model domain to disappear, we obtain 167, 43 and 34 minutes for the approximate half-lives in experiments B, C and D respectively. Although the initial sounding in experiment A is stable, the cloud still loses liquid water due to evaporation induced by entrainment. This rate of loss of liquid water in the stable experiment A is roughly the same as the rate of loss in the unstable experiment B—a fact which underscores the weak nature of the instability in experiment B.

We are now in a position to interpret the observations of persistent stratocumulus on the unstable side of the critical curve in Fig. 1. With soundings such as B, the existence of evaporative instability is not sufficient to guarantee cloud breakup because surface evaporation and upward transport processes can apparently provide enough water vapour to compensate for the evaporative effects associated with the weak evaporative instability. For soundings such as D, the cloud half-life is much smaller, and cloud breakup is to be expected.



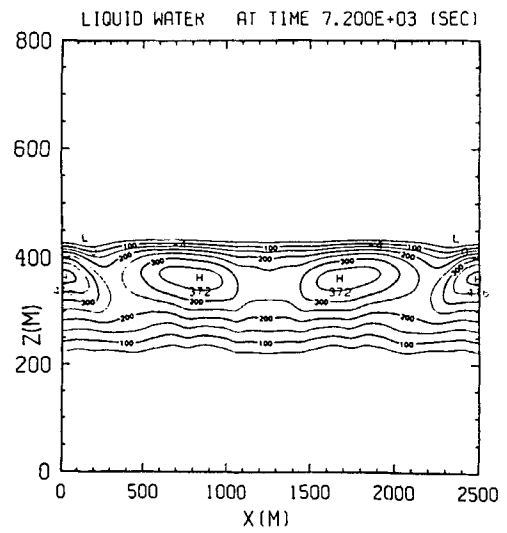
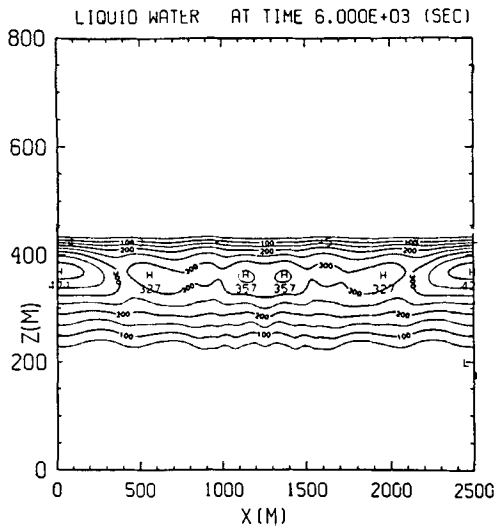
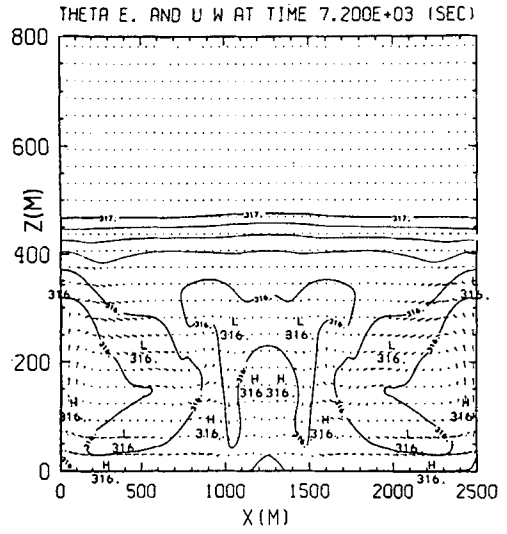
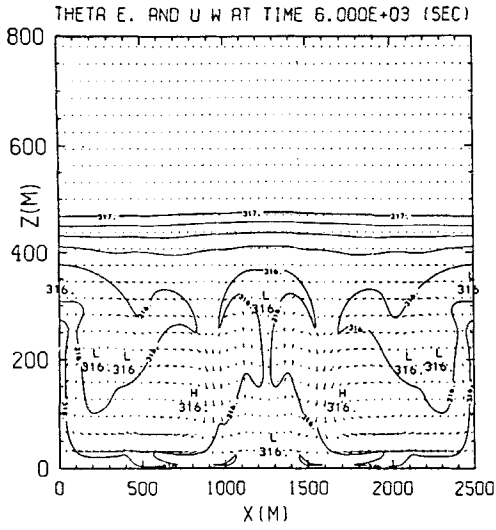




7(c)

7(d)

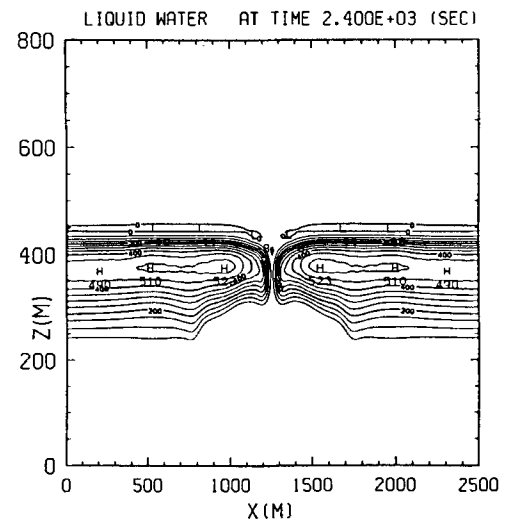
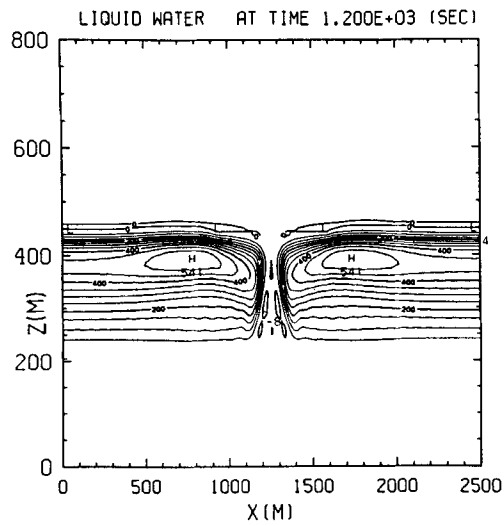
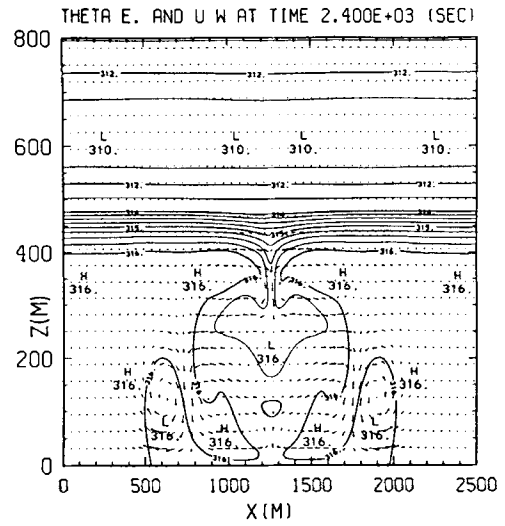
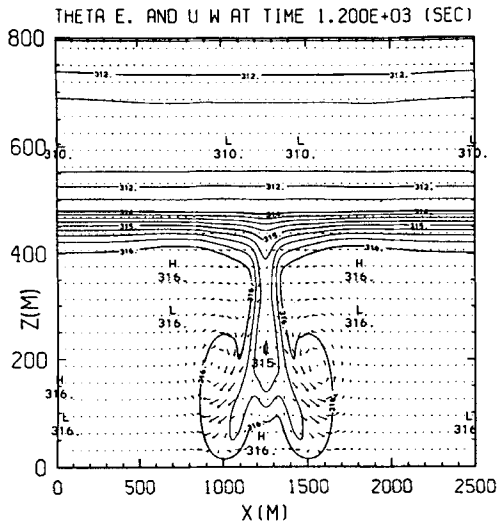
Figure 7 (continued).



7(e)

7(f)

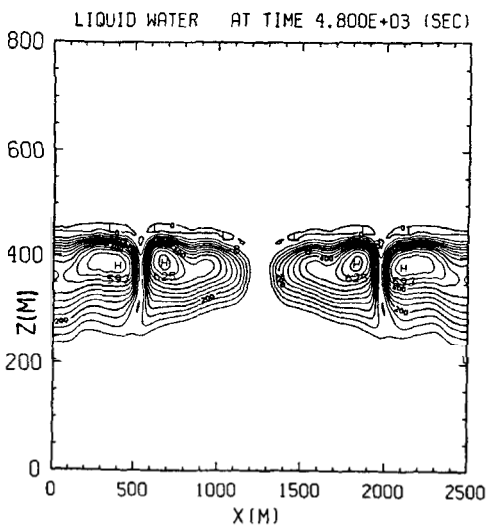
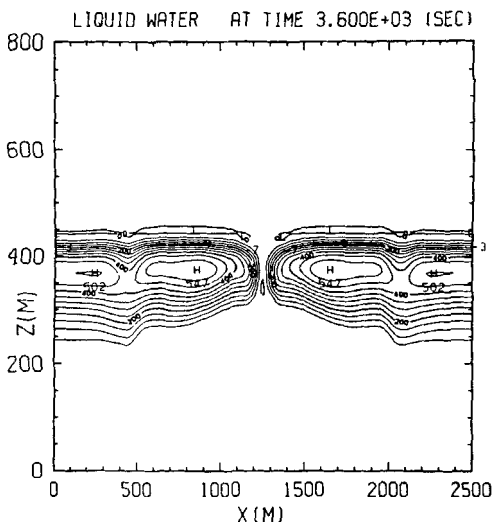
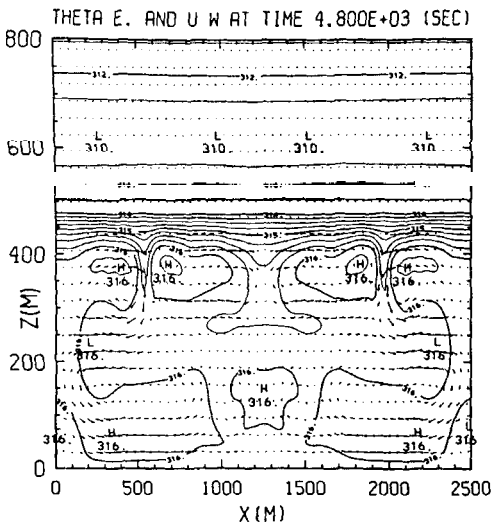
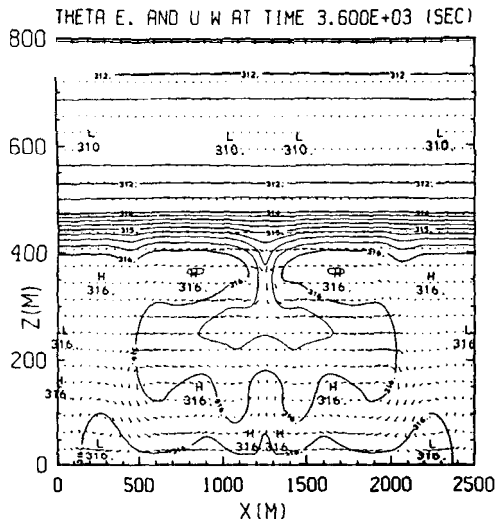
Figure 7 (continued).



8(a)

8(b)

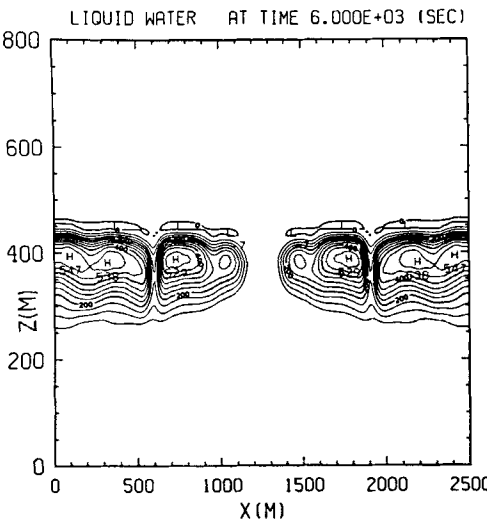
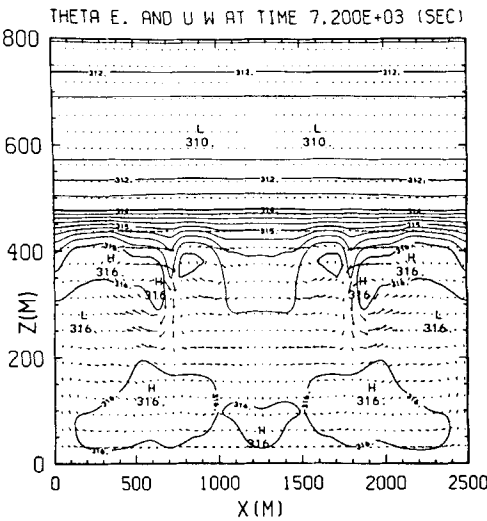
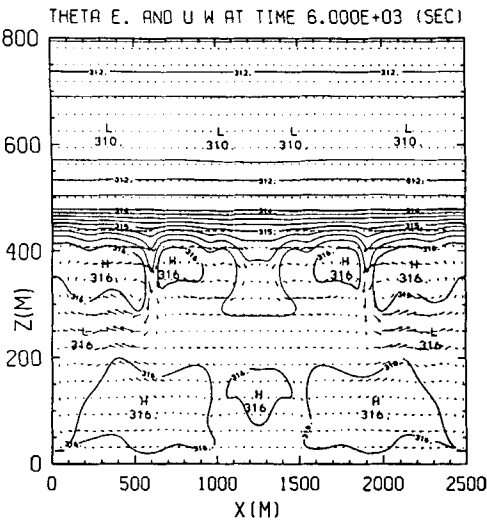
Figure 8. As Fig. 7 but for experiment B. The times and the maximum velocities are as follows: (a) 20 minutes,  $1.03 \text{ m s}^{-1}$ ; (b) 40 minutes,  $0.68 \text{ m s}^{-1}$ ; (c) 60 minutes,  $0.56 \text{ m s}^{-1}$ ; (d) 80 minutes,  $0.49 \text{ m s}^{-1}$ ; (e) 100 minutes,  $0.44 \text{ m s}^{-1}$ ; (f) 120 minutes,  $0.43 \text{ m s}^{-1}$ .



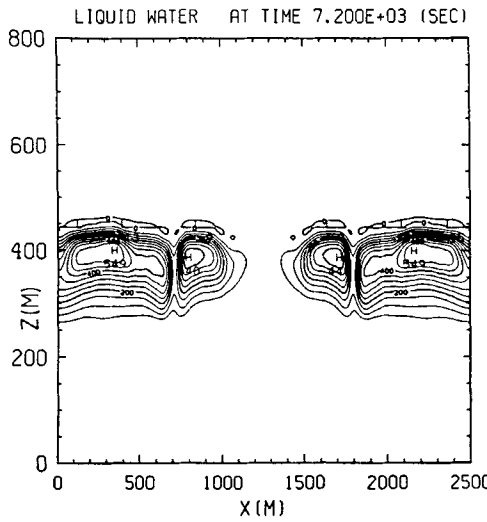
8(c)

8(d)

Figure 8 (continued).



8(e)



8(f)

Figure 8 (continued).

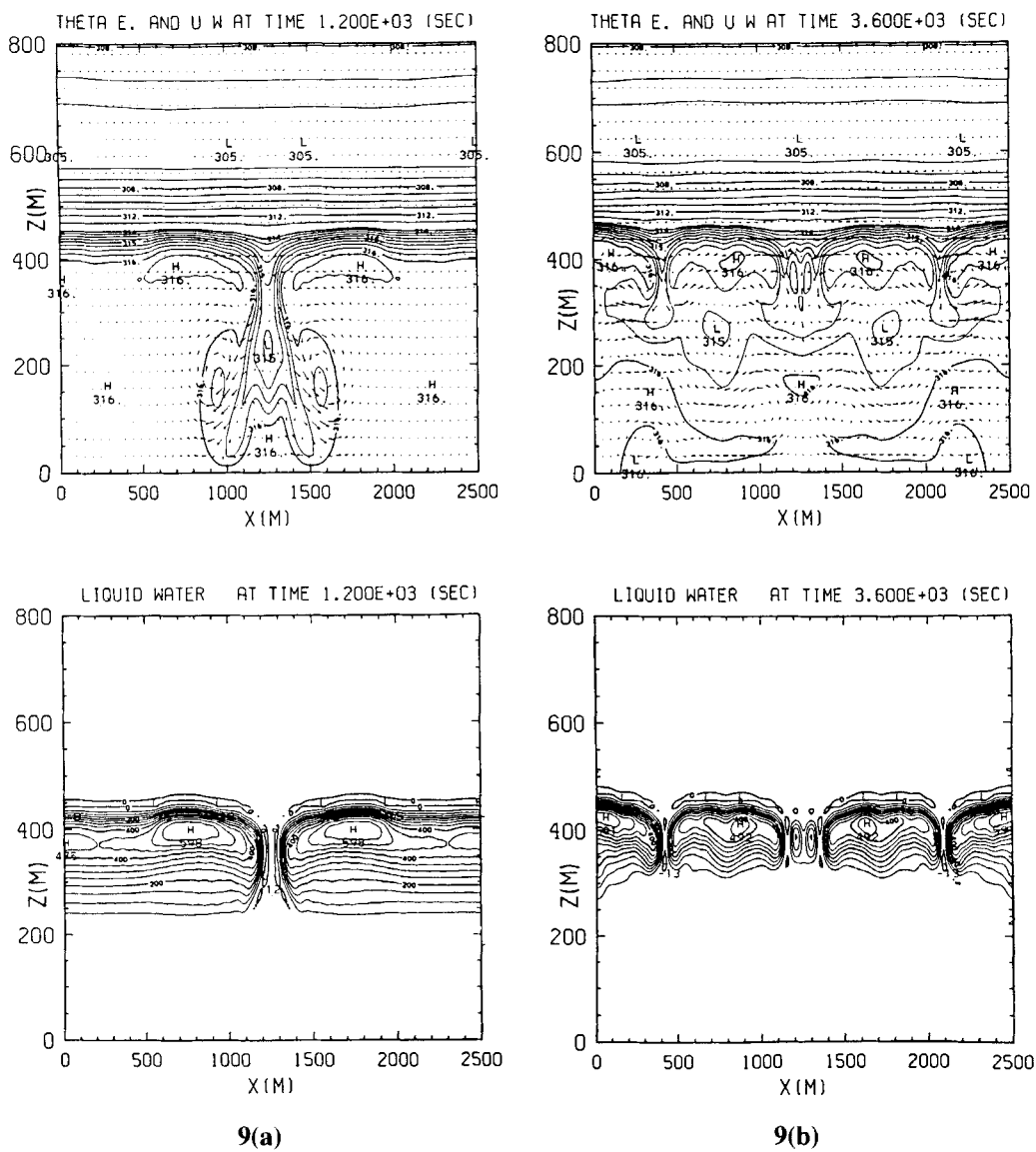
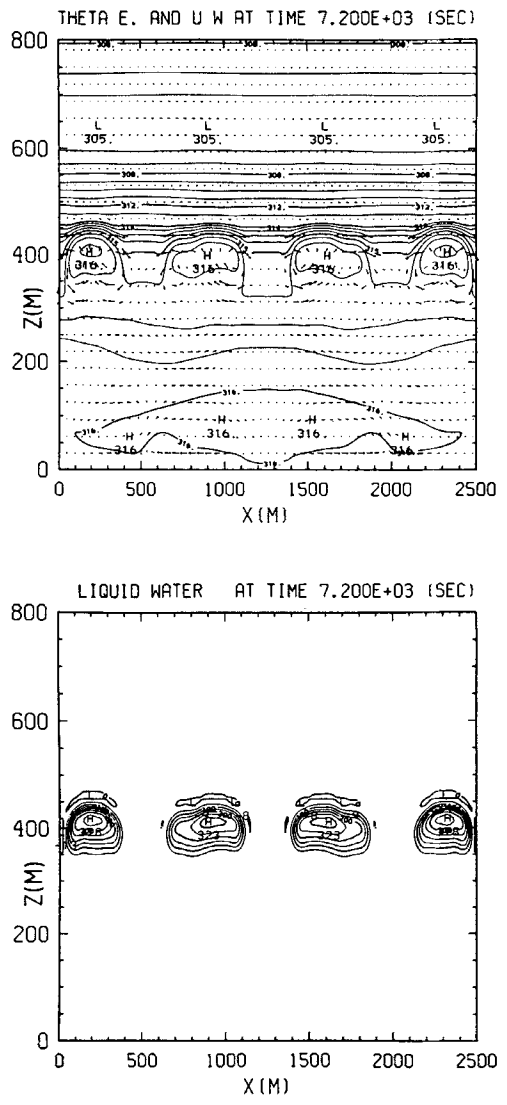


Figure 9. As Fig. 7 but for experiment C. The times and the maximum velocities are as follows:  
 (a) 20 minutes,  $1.04 \text{ m s}^{-1}$ ; (b) 60 minutes,  $0.67 \text{ m s}^{-1}$ ; (c) 120 minutes,  $0.33 \text{ m s}^{-1}$ .



9(c)

Figure 9 (continued).



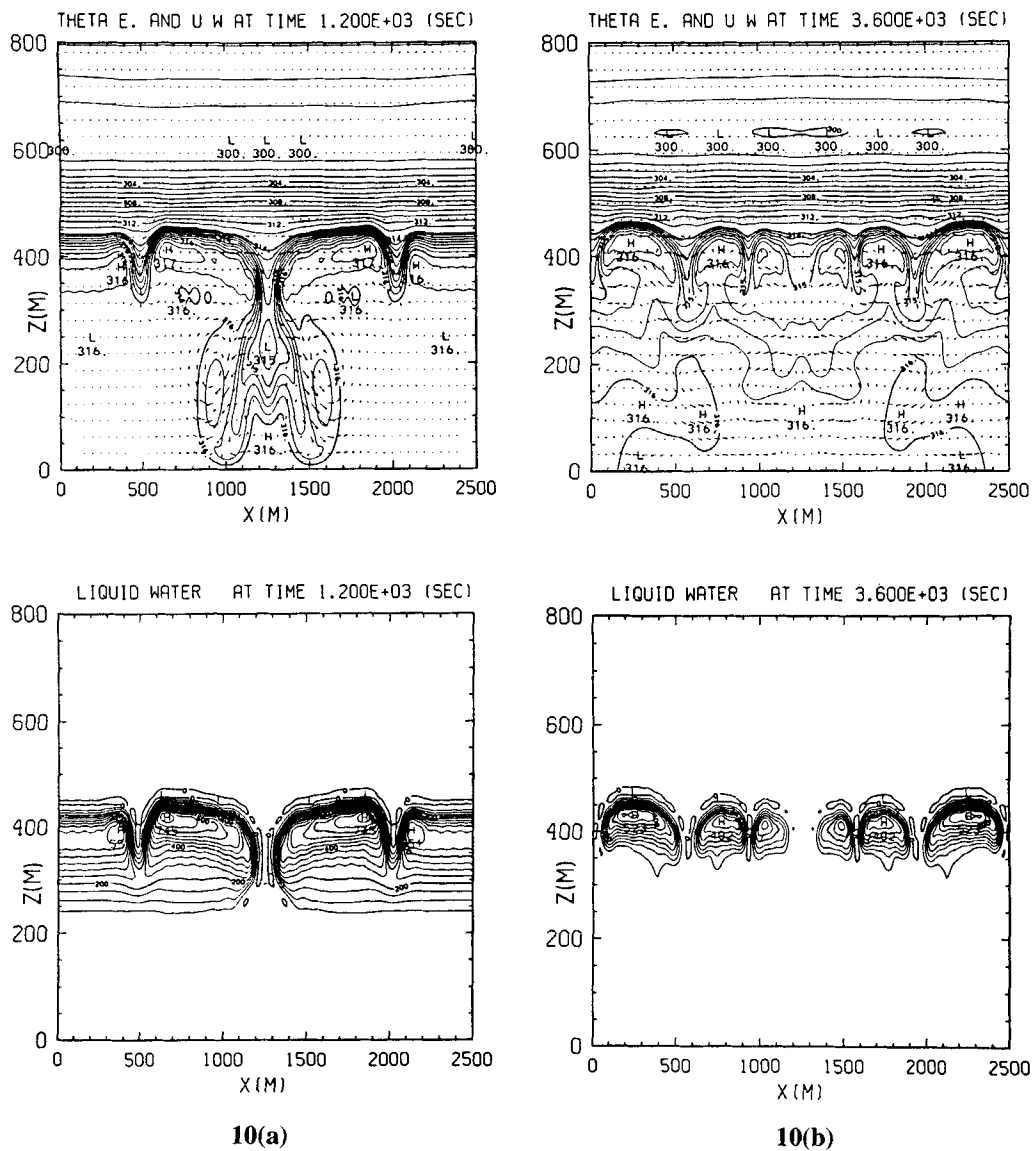


Figure 10. As Fig. 7 but for experiment D. The times and the maximum velocities are as follows: (a) 20 minutes,  $1.10 \text{ m s}^{-1}$ ; (b) 60 minutes,  $0.65 \text{ m s}^{-1}$ ; (c) 120 minutes,  $0.53 \text{ m s}^{-1}$ .



## 5. CONCLUDING REMARKS

Our approach to the evaporative instability problem differs from others which have appeared in the recent literature such as those which use one-dimensional models (e.g. Chen and Cotton 1983) or those which examine much larger horizontal scales of motion (e.g. Moeng and Arakawa 1980). Our approach also differs from that of Deardorff (1980a, b), and it may be of some interest to interpret his experiment in terms of Fig. 1. Deardorff tested the evaporative instability theory using a three-dimensional moist convection model on a  $2\text{ km} \times 2\text{ km} \times 2\text{ km}$  domain with the rather coarse horizontal and vertical resolution of 50 m. Beginning with a sounding which was stable according to (2), he rapidly cooled the air above the cloud in order to induce evaporative instability. In terms of Fig. 1, this procedure can be interpreted as forcing the mean model sounding from the stable point  $(\Delta\theta_e, (L/c_p)\Delta r) = (2.5\text{ K}, -6\text{ K})$  across the stability line to the unstable point  $(\Delta\theta_e, (L/c_p)\Delta r) = (-3\text{ K}, -6\text{ K})$ . During this 90-minute period  $\Delta\theta_i$  decreases from 8.5 K to 3 K, the convective layer deepens from 1450 m to 1800 m, and the entrainment rate increases by a factor of 5.9. Deardorff interpreted this increase in entrainment as due to instability. However, even in the absence of instability, entrainment will increase due to the decrease in  $\Delta\theta_i$ . In order to avoid this ambiguity in interpreting model results and to emulate the organization of the data in Fig. 1, we have chosen our initial value experiments A to D to have identical values of  $\Delta\theta_i$ , with the degree of entrainment instability in the soundings determined entirely by the moisture content of the air above the inversion.

Although we have directed our attention toward stratocumulus clouds, our results may also aid in understanding the structure of cumulus clouds. Recently, Klaassen and Clark (1985) have discovered a cloud top nodal instability in their high resolution two-dimensional model of non-precipitating cumulus convection. Because of this cloud-environment interface instability, simulated small cumulus quickly develop nodes on a previously smooth cloud top. Under certain conditions the growth of these nodes can cause the entrainment and penetration of dry air deep into the cloud interior. Although there are undoubtedly differences in the way instability is triggered in our stratocumulus model and in Klaassen and Clark's cumulus model, there is sufficient gross similarity in the evolution of the flow patterns that we might interpret Klaassen and Clark's results in terms of Fig. 1. Klaassen and Clark's interface instability seems to be enhanced when the smooth cumulus cloud top begins to penetrate into a very dry overlying layer. At this time, the cumulus updraught has brought up air with high  $\theta_e$  and high  $r$  so that it is in contact with the low  $\theta_e$  and low  $r$  overlying air. In terms of cloud top jumps, this corresponds roughly to a situation near point C in Fig. 1. However, liquid water contents in Klaassen and Clark's cumulus simulations are two or three times larger than in our stratocumulus simulations. Thus, the potential for negative buoyancy in the cumulus case is larger than shown in our Fig. 5, a fact which is consistent with the vigorous form of instability in Klaassen and Clark's simulations.

In closing we would like to add the observation that we have chosen to use our computing resources to obtain high resolution two-dimensional simulations rather than lower resolution three-dimensional simulations. Obviously, our conclusions need to be substantiated by high resolution three-dimensional modelling such as that recently performed by Moeng (1986) and by Tag and Payne (1987).

## ACKNOWLEDGMENTS

The authors would like to thank Scott Fulton for providing the package of Chebyshev routines used here, Alan Betts for first pointing out the importance of including the trade

cumulus data in Fig. 1, Clark Weaver and Chi-Fan Shih for providing the 1985 Electra and GOES satellite data, and Thomas Vonder Haar, Richard Johnson, Gerald Taylor, George Young, Terry Clark, Philip Durkee and Paul Ciesielski for helpful discussions.

Development of the spectral methods used here has been supported by NSF grant ATM-8510664 and ONR grant N00014-87-K-0535. The field and analysis phases of the FIRE marine stratocumulus project have been supported by ONR grant N00014-87-K-0228. Acknowledgment is also made to the National Center for Atmospheric Research, which is sponsored by the National Science Foundation, for computer time used in this research.

#### APPENDIX

Equations (27)–(30) are obtained by taking the Fourier–Chebyshev inner product (defined by (24)) of each of the equations (14)–(17) with the basis function  $T_n(z')e^{2\pi imx/L}$ . For example, from (15) we obtain (28) with  $\hat{A}_{mn}^{(1,0)}$ ,  $\hat{D}_{mn}^{(0,1)}$  and  $\hat{\theta}_{vmn}^{(1,0)}$  given by

$$\hat{A}_{mn}^{(1,0)} = \frac{2}{\pi c_n} \left\langle \frac{\partial A}{\partial x}, T_n(z')e^{2\pi imx/L} \right\rangle = i \left( \frac{2\pi m}{L} \right) \hat{A}_{mn} \quad (\text{A.1})$$

$$\hat{B}_{mn}^{(0,1)} = \frac{2}{\pi c_n} \left\langle \frac{\partial B}{\partial z}, T_n(z')e^{2\pi imx/L} \right\rangle \quad (\text{A.2})$$

$$\hat{\theta}_{vmn}^{(1,0)} = \frac{2}{\pi c_n} \left\langle \frac{\partial \theta_v}{\partial x}, T_n(z')e^{2\pi imx/L} \right\rangle = i \left( \frac{2\pi m}{L} \right) \hat{\theta}_{vmn}. \quad (\text{A.3})$$

To evaluate (A.2) we substitute the Fourier–Chebyshev expansion for B to obtain

$$\hat{B}_{mn}^{(0,1)} = \frac{4}{H\pi c_n} \sum_{m'=-M}^M \sum_{n'=0}^N \hat{B}_{m'n'} \left\langle \frac{\partial T_{n'}(z')}{\partial z'} e^{2\pi im'x/L}, T_n(z')e^{2\pi imx/L} \right\rangle. \quad (\text{A.4})$$

Using the Chebyshev derivative relation

$$\frac{\partial T_n(z')}{\partial z'} = \begin{cases} 2n(T_{n-1} + T_{n-3} + \cdots + T_3 + T_1) & n \text{ even} \\ 2n(T_{n-1} + T_{n-3} + \cdots + T_4 + T_2) + nT_0 & n \text{ odd} \end{cases} \quad (\text{A.5})$$

it is easy to show that

$$\left\langle \frac{\partial T_{n'}(z')}{\partial z'} e^{2\pi im'x/L}, T_n(z')e^{2\pi imx/L} \right\rangle = \begin{cases} n'\pi & m' = m \text{ and } n' + n \text{ odd, } n < n' \\ 0 & \text{otherwise} \end{cases} \quad (\text{A.6})$$

which allows (A.4) to be written as

$$\hat{B}_{mn}^{(0,1)} = \frac{4}{Hc_n} \sum_{\substack{n'=n+1 \\ n'+n \text{ odd}}}^N n' \hat{B}_{mn'}. \quad (\text{A.7})$$

The derivations of (29) and (30) proceed similarly. The derivation of (27) involves second derivatives. Taking the Fourier–Chebyshev inner product of (14) with  $T_n(z')e^{2\pi imx/L}$  we obtain

$$\frac{2}{\pi c_n} \left\langle \frac{\partial^2 \psi}{\partial z^2}, T_n(z')e^{2\pi imx/L} \right\rangle - \left( \frac{2\pi m}{L} \right)^2 \hat{\psi}_{mn} = \hat{\xi}_{mn}. \quad (\text{A.8})$$

To evaluate the first term we substitute the Fourier–Chebyshev expansion for  $\psi$  to obtain

$$\left\langle \frac{\partial^2 \psi}{\partial z^2}, T_n(z') e^{2\pi i m x/L} \right\rangle = \left( \frac{2}{H} \right)^2 \sum_{m'=-M}^M \sum_{n'=0}^N \hat{\psi}_{m'n'} \left\langle \frac{\partial^2 T_{n'}(z')}{\partial z'^2} e^{2\pi i m' x/L}, T_n(z') e^{2\pi i m x/L} \right\rangle. \quad (\text{A.9})$$

Differentiating (A.5) with respect to  $z'$  and then using (A.5) itself, it can be shown that

$$\left\langle \frac{\partial^2 T_{n'}(z')}{\partial z'^2} e^{2\pi i m' x/L}, T_n(z') e^{2\pi i m x/L} \right\rangle = \begin{cases} (\pi/2) n' (n'^2 - n^2) & m' = m \text{ and } n' + n \text{ even, } n + 1 < n' \\ 0 & \text{otherwise} \end{cases} \quad (\text{A.10})$$

which allows (A.8) to be written

$$\frac{4}{H^2 c_n} \sum_{\substack{n'=n+2 \\ n'+n \text{ even}}}^N n' (n'^2 - n^2) \hat{\psi}_{mn'} - \left( \frac{2\pi m}{L} \right)^2 \hat{\psi}_{mn} = \xi_{mn}. \quad (\text{A.11})$$

Equation (A.11) is required to hold for  $n = 0, 1, 2, \dots, N-2$ . The boundary conditions  $\psi(x, 0, t) = \psi(x, H, t) = 0$  are then used to close the system.

#### REFERENCES

- |  |       |   |
|--|-------|---|
| Albrecht, B. A., Penc, R. S. and Schubert, W. H.     | 1985  | An observational study of cloud-topped mixed layers. <i>J. Atmos. Sci.</i> , <b>42</b> , 800–822  |
| Augstein, E., Riehl, H., Ostapoff, F. and Wagner, V. | 1973  | Mass and energy transports in an undisturbed Atlantic trade wind flow. <i>Mon. Weather Rev.</i> , <b>101</b> , 101–111  |
| Betts, A. K., and Albrecht, B. A.                    | 1987  | Conserved variable analysis of the convective boundary layer thermodynamic structure over the tropical oceans. <i>J. Atmos. Sci.</i> , <b>44</b> , 83–99  |
| Chen, C. and Cotton, W. R.                           | 1983  | A one-dimensional simulation of the stratocumulus-capped mixed layer. <i>Boundary-Layer Meteorol.</i> , <b>25</b> , 289–321   |
| Davis, P. J. and Rabinowitz, P.                      | 1984  | <i>Methods of numerical integration</i> . Academic Press  |
| Deardorff, J. W.                                     | 1980a | Cloud-top entrainment instability. <i>J. Atmos. Sci.</i> , <b>37</b> , 131–147  |
|  | 1980b | Stratocumulus-capped mixed layers derived from a three-dimensional model. <i>Boundary-Layer Meteorol.</i> , <b>18</b> , 495–527   |
| Eliassen, E., Machenhauer, B. and Rasmussen, E.      | 1970  | 'On a numerical method for integration of the hydrodynamical equations with a spectral representation of the horizontal fields'. Report No. 2, Institut for Teoretisk Meteorologi, Kobenhavns Universitet |
| Fulton, S. R. and Schubert, W. H.                    | 1987a | Chebyshev spectral methods for limited-area models. I: Model problem analysis. <i>Mon. Weather Rev.</i> , <b>115</b> , 1940–1953  |
|  | 1987b | Chebyshev spectral methods for limited-area models. II: Shallow water model. <i>ibid.</i> <b>115</b> , 1954–1965  |
| Gerber, H.   | 1986  | 'Tethered balloon measurements at San Nicolas Island (Oct. 1984): Instrumentation, data summary, preliminary data interpretation'. Naval Research Laboratory Report 8972                                  |
| Gottlieb, D. and Orszag, S. A.                       | 1977  | 'Numerical analysis of spectral methods'. NSF-CBMS Monograph No. 26, NTIS No. AD-A056 922, Soc. Ind. and Appl. Math., Philadelphia  |
| Hanson, H. P.  | 1984  | On mixed-layer modeling of the stratocumulus-topped marine boundary layer. <i>J. Atmos. Sci.</i> , <b>41</b> , 1226–1234  |
| Holland, J. Z. and Rasmusson, E.                     | 1973  | Measurements of the atmospheric mass, energy and momentum budgets over a 500 km square of tropical ocean. <i>Mon. Weather Rev.</i> , <b>101</b> , 44–55   |
| Klaassen, G. P. and Clark, T. L.                     | 1985  | Dynamics of the cloud–environment interface and entrainment in small cumuli: Two-dimensional simulations in the absence of ambient shear. <i>J. Atmos. Sci.</i> , <b>42</b> , 2621–2642                   |

- Langlois, W. E. 1973 A rapidly convergent procedure for computing large-scale condensation in a dynamical weather model. *Tellus*, **25**, 86–87
- Lilly, D. K. 1968 Models of cloud-topped mixed layers under a strong inversion. *Q. J. R. Meteorol. Soc.*, **94**, 292–309
- Machenhauer, B. 1979 *Numerical methods used in atmospheric models*. Vol. II, chapter 3: The spectral method. GARP Publication Series No. 17
- Moeng, C.-H. 1986 Large-eddy simulation of a stratus-topped boundary layer. Part I: Structure and budgets. *J. Atmos. Sci.*, **43**, 2886–2900
- Moeng, C.-H. and Arakawa, A. 1980 A numerical study of a marine subtropical stratus cloud layer and its stability. *ibid.*, **37**, 2661–2676
- Nicholls, S. and Leighton, J. 1986 An observational study of the structure of stratiform cloud sheets: Part I: Structure. *Q. J. R. Meteorol. Soc.*, **112**, 431–460
- Nicholls, S. and Turton, J. D. 1986 An observational study of the structure of stratiform cloud sheets: Part II: Entrainment. *ibid.*, **112**, 461–480
- Ogura, Y. and Phillips, N. A. 1962 Scale analysis of deep and shallow convection in the atmosphere. *J. Atmos. Sci.*, **19**, 173–179
- Orszag, S. A. 1970 Transform method for the calculation of vector-coupled sums: Application to the spectral form of the vorticity equation. *ibid.*, **27**, 890–895
- Randall, D. A. 1980 Conditional instability of the first kind upside-down. *ibid.*, **37**, 125–130
- Rogers, D. P. and Telford, J. W. 1986 Metastable stratus tops. *Q. J. R. Meteorol. Soc.*, **112**, 481–500
- Schubert, W. H., Ciesielski, P. E., 1987a 'Analysis of boundary layer sounding data from the FIRE marine stratocumulus project'. Colorado State University Atmospheric Science Paper No. 419
- McKee, T. B., Kleist, J. D., Cox, S. K., Johnson-Pasqua, C. M. and Smith, W. L. Jr. 1987b 'Operation of a ceilometer during the FIRE marine stratocumulus experiment'. Colorado State University Atmospheric Science Paper No. 420
- Slingo, A., Nicholls, S. and Johnson-Pasqua, C. M. 1982a Aircraft observations of marine stratocumulus during JASIN. *Q. J. R. Meteorol. Soc.*, **108**, 833–856
- Slingo, A., Brown, R. and Schmetz, J. 1982b A field study of nocturnal stratocumulus. Part III. High resolution radiative and microphysical observations. *ibid.*, **108**, 145–165
- Squires, P. 1958 Penetrative downdraughts in cumuli. *Tellus*, **10**, 381–389
- Tag, P. M. and Payne, S. W. 1987 An examination of the breakup of marine stratus: A three-dimensional numerical investigation. *J. Atmos. Sci.*, **44**, 208–223
- Taylor, P. K., Grant, A. L. M., 1983 Mass, momentum, sensible heat and latent heat budgets for the lower atmosphere. *Phil. Trans. R. Soc. London*, **A**, **308**, 275–290
- Gunther, H. and Olbruck, G.
- Weaver, C. J. 1987 'Observational analysis of cumulus and stratocumulus entrainment using ozone'. Ph.D. dissertation. Department of Atmospheric Science, Colorado State University